Vesiculation pathways in clathrin-mediated endocytosis

Xinran Wang[a,b], **Julien Berro**[c,d,e,1], **and Rui Ma**[a,b,1]

[a]Department of Physics, Xiamen University, Xiamen 361005, China; [b]Fujian Provincial Key Lab for Soft Functional Materials Research, Xiamen University, 361005, China; [c]Department of Molecular Biophysics and Biochemistry, Yale University, New Haven, CT 06520, USA; [d]Nanobiology Institute, Yale University, West Haven, CT 06516, USA; [e]Department of Cell Biology, Yale University School of Medicine, New Haven, CT 06520, USA

This manuscript was compiled on August 13, 2024

During clathrin-mediated endocytosis, a patch of flat plasma membrane is internalized to form a vesicle. In mammalian cells, how the clathrin coat deforms the membrane into a vesicle remains unclear and two main hypotheses have been debated. The "constant area" hypothesis assumes that clathrin molecules initially form a flat lattice on the membrane and deform the membrane by changing its intrinsic curvature while keeping the coating area constant. The alternative "constant curvature" hypothesis assumes that the intrinsic curvature of the clathrin lattice remains constant during the formation of a vesicle while the surface area it covers increases. Previous experimental studies were unable to unambiguously determine which hypothesis is correct. In this paper, we show that these two hypotheses are only two extreme cases of a continuum of vesiculation pathways if we account for the free energies associated with clathrin assembly and curvature generation. By tracing the negative gradient of the free energy, we define vesiculation pathways in the phase space of the coating area and the intrinsic curvature of clathrin coat. Our results show that, overall, the differences in measurable membrane morphologies between the different models are not as big as expected, and the main differences are most salient at the early stage of endocytosis. Furthermore, the best fitting pathway to experimental data is not compatible with the constant-curvature model and resembles to a constant-area-like pathway where the coating area initially expands with minor changes in the intrinsic curvature, later followed by a dramatic increase in the intrinsic curvature and minor change in the coating area. Our results also suggest that experimental measurement of the tip radius and the projected area of the clathrin coat will be the key to distinguish between models.

Endocytosis | Vesiculation | Clathrin assembly | Curvature generation

Clathrin-mediated endocytosis (CME) is a fundamental cellular process to transport lipids, membrane proteins and extracellular cargo molecules into the cell (1–6). In mammalian cells, a small patch of flat plasma membrane is shaped into a spherical vesicle when CME occurs (7). Clathrin molecules are essential for the membrane remodelling process. They are made of three subunits that form a triskelion, which further assemble into a cage-like structure *in vitro* (8, 9). The minimum cages contain 16 polygons (10) and the most commonly observed ones are semi-regular icosahedral cages (11–13). Two main hypotheses are under debate regarding how the clathrin coat scaffolds the flat membrane into a spherical vesicle *in vivo* (4, 7, 14–16). The **constant area model** asserts that the clathrin molecules initially polymerize into a flat lattice with a regularly arranged hexagonal structure, and later reorganization of the bonds between adjacent clathrins results in formation of pentagons in the hexagonal lattice, which in turn leads to curvature generation of the clahtrin coat (10, 17) (Fig. 1a). Adhesion of clathrin molecules with the substrate has been suggested to contribute a flattening force that prevents curvature generation. Release of the flattening force therefore could induce curvature of the clathrin coat with preloaded pentagons (18). The alternative **constant curvature model** asserts that the intrinsic curvature of the elements of the lattice is kept constant during the assembly and expansion of the lattice, therefore curvature generation occurs from the very beginning of clathrin assembly (Fig. 1b).

In order to distinguish between the two models, the dynamics of clathrin assembly and the geometry of membrane shapes are needed. Fluorescence microscopy, including light sheet and MINFLUX, has revealed the assembly dynamics of the clathrin coat (19, 20), as well as other proteins that participate in endocytosis (21–27), while electron tomography has been able to resolve membrane shapes during endocytosis (7, 28). However, neither of the methods can capture both spatial and temporal information at the same time. Under conventional fluorescence microscopy, the clathrin-coated pits appear as diffraction-limited spots due to their small size (typically $\sim 30-150$nm in mammals (1) and yeast (28)) and shape information of the membrane is completely lost (21, 29–32). On the other hand, super-resolution fluorescence microscopy has been able to reveal the protein organization at the endocytic pit (29, 33, 34) and to reconstruct the shape of the clathrin coat (16, 35, 36) from averaging over ensembles of endocytic sites. Correlative light and electron microscopy (CLEM) method has exploited the fluorescence of fiducial markers to locate endocytic sites while resolving membrane shapes using elec-

Significance Statement

Endocytosis is a fundamental cellular process for cells to communicate with their environment and recycle their membrane components. How clathrin molecules remodel the membrane remains debated more than 30 years after the discovery of clathrin. Whether curvature generation happens at the early stage of clathrin assembly or at the late stage is at the center of the debate. We constructed a physical model which allowed us to calculate an optimum pathway that is actually a combination of these two extreme hypotheses, and is closer to the late stage hypothesis than to the early stage hypothesis. Our results also suggest future experiments that can distinguish between the different hypotheses.

R.M. and J.B. designed the research; R.M. performed the research; R.M. and X.W. analyzed the data; R.M., J.B. and X.W. wrote the paper.

The authors declare no competing interests.

[1]To whom correspondence should be addressed. E-mail: ruima@xmu.edu.cn, julien.berro@yale.edu

tron tomography. However, both super-resolution and CLEM requires sample fixation, therefore, one can identify multiple endocytic sites at the same time and perform the average, yet unable to trace a single endocytic site over time. The temporal information is nevertheless lost. As a result of the incomplete information obtained by existing experimental methods, both hypotheses have experimental support. Experiments that apply electron microscopy to resolve the membrane shapes of endocytic pits favor the constant area model (7, 18, 37, 38). However, super-resolution imaging combined with analysis of the fluorescence intensity of the clathrin coat is inclined towards the constant curvature model (39). In addition, it was argued that the energetic cost of bond reorganization in a regular hexagonal lattice in the constant area model may be too large to be fulfilled (15, 40, 41).

Extensive theoretical efforts have been dedicated to model membrane morphology during endocytosis (42), of which molecular dynamics simulations (43) and continuum mechanics (44–48) are two common approaches. Hybrid models were also broadly applied to gain higher resolution than continuum mechanics and lower computing expense than molecular dynamics (49, 50). However, most theoretical investigations have focused on how mechanical properties, such as membrane tension and bending rigidity of the clathrin coat, influence the membrane morphology. The process of curvature generation is either neglected or taken for granted. Only few of them have addressed the difference between the constant area model and the constant curvature model.

In fact, the constant curvature and constant area models are only two extreme models for clathrin assembly during endocytosis and any change in area or curvature are possible at any time point during endocytosis. In this paper, we extend the classic Helfrich theory for membrane deformation to incorporate energy terms associated with clathrin assembly and curvature generation, and compare geometric features calculated by theory with that extracted from experimental data. The negative gradient of the total free energy defines a pathway that neither fits the constant area model nor the constant curvature model. We find that a pathway that is close to the constant area model fits electron tomograms of the endocytic pits the best. Our study also offers experimental suggestions to distinguish between the two main hypotheses.

Models and methods

We model the membrane patch of the CCP (clathrin-coated pit) as a surface which is rotationally symmetric with respect to the z-axis. The shape of the membrane is parameterized with the meridional curve $\{r(s), z(s)\}$, where s denotes the arc length along the curve. The bending energy of the membrane (together with the clathrin coat) assumes the Helfrich model (51)

$$E_{\rm b} = \int \frac{\kappa}{2}(C_1 + C_2 - C_0)^2 {\rm d}a, \qquad [1]$$

where κ denotes the bending rigidity of the CCP, C_1 and C_2 denote the principal curvatures of the surface, C_0 denotes the intrinsic curvature of the membrane induced by the clathrin coat. To model a finite area of the clathrin coat, we assume the intrinsic curvature C_0 spatially varies as

$$C_0(a) = \frac{1}{2}c_0(1 - \tanh[\alpha(a - a_0)]), \qquad [2]$$

where a denotes positions on the membrane. Here we choose a to be the surface area calculated from the tip of the membrane, and C_0 equals c_0 for area $a < a_0$, and rapidly drops to zero when $a > a_0$. The parameter α controls the sharpness of the drop. In the constant area model, we vary the intrinsic curvature c_0 but keep the coating area a_0 constant, while in the constant curvature model, we vary the coating area a_0 but keep the intrinsic curvature c_0 constant. As a result of clathrin coat, the bending rigidity κ also varies as

$$\kappa(a) = \frac{1}{2}(\kappa_{\rm coat} - \kappa_{\rm bare})(1 - \tanh[\alpha(a - a_0)]) + \kappa_{\rm bare}, \qquad [3]$$

where $\kappa_{\rm coat}$ and $\kappa_{\rm bare}$ denotes the bending rigidity of the clathrin-coated membrane and bare membrane, respectively. Besides the bending energy, the membrane tension contributes to the free energy in the form of

$$E_{\rm t} = \sigma_{\rm e} A, \qquad [4]$$

where $\sigma_{\rm e}$ denotes the membrane tension at the base and A denotes the surface area of the membrane patch within a fixed radius of $R_{\rm b}$. The membrane tension $\sigma_{\rm e}$ and bending rigidity κ defines a characteristic length $L_0 = \sqrt{\kappa_{\rm bare}/(2\sigma_{\rm e})}$ (52). The total free energy $E_{\rm tot} = E_{\rm b} + E_{\rm t}$ is a functional of the membrane shape. Given a coating area a_0 and an intrinsic curvature c_0, we numerically solve the variational equations of the energy functional to obtain membrane shapes that minimizes $E_{\rm tot}$. More detailed descriptions of the model can be found in SI Appendix: detailed formula derivation.

Results

Difference between the constant area model and the constant curvature model in terms of membrane morphology. Vesiculation requires assembly of a clathrin coat on the membrane, as well as curvature generation from the clathrin coat. A vesiculation process defines a pathway in the phase space (a_0, c_0) of the clathrin coat area a_0 and the intrinsic curvature c_0 of the coat. The constant area model and the constant curvature model are pathways that are made of a vertical line and a horizontal line. Besides these two extreme cases, there is a continuum spectrum of pathways with simultaneously increasing coating area a_0 and intrinsic curvature c_0 that could lead to vesiculation. Along the pathway, the membrane evolves from a flat shape to a dimple shape, and finally to an Ω-shape, as shown in Fig. 2. Hereafter we use the maximal tangential angle $\psi_{\rm max}$ of the membrane as an indicator of the progression of vesiculation - when the membrane is flat, $\psi_{\rm max} = 0°$, and when the membrane becomes spherical, $\psi_{\rm max} = 180°$. In our simulation, the neck becomes extremely narrow before $_{\rm max} = 180°$. Therefore, we consider vesiculation occurs when $_{\rm max}$ reaches 150° (Fig. 2a).

First, we analyze the difference between the two models in terms of membrane morphology evolution along their pathways. We fit a circle around the membrane tip and use the radius $R_{\rm t}$ of the circle to characterize the curvature of the membrane at the tip. When $R_{\rm t}$ is plotted against the maximal angle $_{\rm max}$, both models show that $R_{\rm t}$ decreases with increasing $_{\rm max}$ (Fig. 2b and c). We stress that even though the intrinsic curvature c_0 is fixed in the constant curvature model, it does not imply the tip radius along the vesiculation pathway is a constant. When the coating area is small, the geometric curvature at the membrane tip remains small and differs from

the intrinsic curvature. Tip radius in the constant curvature model decays more steeply with $\psi_{\max}$ than in the constant area model. This difference becomes obvious when one plots the ratio of the tip radius at $\psi_{\max} = 150^\circ$ and $\psi_{\max} = 30^\circ$ (Fig. 2b and c insets). For the constant area model, the ratio approximately equals to a constant 0.268 regardless of the coating area a_0, which agrees well with the analytical result (See SI Appendix: model fitting), while for the constant curvature model, the ratio stays above 0.6 and approaches 1 at a certain c_0 value.

Another difference between the two models is the evolution of the projected area of the clathrin coat on the substrate. We use the maximal radius R_{coat} of the membrane within the clathrin-coated area as the indicator of the projected area (Fig. 2a). In the constant area model, R_{coat} decreases with increasing $\psi_{\max}$, while in the constant curvature model, R_{coat} increases with $\psi_{\max}$ and reaches a plateau (Fig. 2d and e). The ratio $R_{\text{coat}}(150^\circ)/R_{\text{coat}}(90^\circ)$ is about 0.732 in the constant area model and around 1 in the constant curvature model (Fig. 2d and e, insets). The analytical curves of R_{t} and R_{coat} against $\psi_{\max}$ also fit perfectly with numerical solutions in the constant area model (Fig. 2b and d, compare dotted and solid curves). Our calculations therefore demonstrate that the two models exhibit clear differences in the evolution of R_{t} and R_{coat} at the beginning of endocytosis (i.e. when $\psi_{\max}$ is small) which can be determined from shapes of endocytic pits obtained experimentally.

To demonstrate how the coating area a_0 and the intrinsic curvature c_0 of the clathrin coat influence the membrane morphology, for each pair of (a_0, c_0), we calculate the corresponding membrane shapes and plot the contour lines for $\psi_{\max}$ which indicate the stage of endocytosis (Fig. 2f). The contour line with $\psi_{\max} = 150^\circ$ represents the critical line where vesiculation occurs. The line can be well fitted by the analytical expression $\bar{a}_0\bar{c}_0^2 = 8$ (Fig. 2f, thick black line, see SI Appendix: critical vesiculation curve). It implies that a small intrinsic curvature of the clathrin coat is able to induce vesiculation of the membrane with a large clathrin coat. We find that the distances between contour lines for higher values of $\psi_{\max}$ is smaller than those for lower values of $\psi_{\max}$. It means that at the late stage of endocytosis, a small change in a_0 and c_0 could result in a more dramatic change in the membrane shape than that at the early stage. This trend is demonstrated clearly from the orange dots in Fig. 2f, which correspond to shapes in Fig. 2a.

Note that in order to produce the diagram in Fig. 2f, it requires that the bending rigidity of the clathrin coated area κ_{coat} is significantly larger than κ_{bare} in the uncoated area. If κ_{coat} is comparable with κ_{bare}, there exists a region in the phase diagram in which a single (a_0, c_0) corresponds to three possible membrane shapes (See Fig. S1 a-d). Physically, it implies a discontinuous transition in the membrane shape along a path that passes through this region, and a gap in the maximal angle $\psi_{\max}$ would appear. Because in experiments, a wide spectrum of $\psi_{\max}$ are observed and no gap in $\psi_{\max}$ is found (7), we keep κ_{coat} much greater than κ_{bare} for the rest of the paper. In this regime, the membrane shapes evolve continuously along any pathway that connects the origin $(0, 0)$ with a point on the critical vesiculation curve.

Vesiculation needs free energy sources to drive clathrin assembly and curvature generation. In the previous section, we take curvature generation in the constant area model and clathrin assembly in the constant curvature model for granted, so that the coating area a_0 and the intrinsic curvature c_0 are imposed, such that the physical forces behind clathrin assembly and curvature generation are ignored. However, the bending energy E_{b} and the tension energy E_{t} typically increase with a_0 and c_0 along a vesiculation pathway. Therefore, vesiculation will be energetically unfavorable if no additional free energy sources are provided. In this section, we extend the model to include free energy terms for the assembly of the clathrin coat and its reorganization for curvature generation.

To describe the assembly of the clathrin coat in the constant curvature model, we introduce

$$E_{\text{a}} = -\mu a_0, \qquad [5]$$

where μ denotes the effective surface binding energy density of clathrin molecules with the membrane. This term reduces the free energy with increasing a_0, therefore, driving the growth of a_0, i.e., clathrin assembly. We can identify three types of free energy curves for different assembly strength μ: (1) When μ is small, the total free energy $E_{\text{tot}} = E_{\text{b}} + E_{\text{t}} + E_{\text{a}}$ as a function of the coating area a_0 has two local minima, with the lowest one at a small a_0 and the other one at the maximum a_0 where vesiculation occurs (Fig. 3a, red curve). The minima are separated by an energy barrier that is significantly higher than the thermal energy $k_{\text{B}}T$ and the clathrin coat would assemble to a small area and halt. (2) With increasing μ, the lowest free energy minimum is shifted to the vesiculation point, but the energy barrier still exists and the clathrin coat remains small (Fig. 3a, orange curve). (3) Vesiculation could happen for large enough μ such that the energy barrier vanishes and the free energy E_{tot} monotonically decreases with a_0 (Fig. 3a, green). Based on the above analysis of the energy landscape we construct the phase diagram of the constant curvature model with clathrin assembly in the phase space of (c_0, μ) and classify the points into four types. Besides the three types mentioned above, when the intrinsic curvature c_0 is small, increasing a_0 to its maximum value (10^5nm^2) cannot produce vesiculation. (Fig. 3b, gray region). The critical assembly energy density μ at which the energy barrier vanishes is found to increase with the intrinsic curvature c_0 (Fig. 3b, interface between the green region and the orange region), which implies that a larger assembly strength of clathrin coat μ is needed to complete vesiculation if the clathrin coat has a higher intrinsic curvature c_0. When comparing the contour lines of the energy barrier $\Delta E_{\text{tot}} = 1k_{\text{B}}T$ and $\Delta E_{\text{tot}} = 10k_{\text{B}}T$ (Fig. 3b, dotted curve and dash-dotted curve), the gap between them increases with c_0, which means that the energy efficiency is reduced with c_0 in the sense that, for larger c_0, a larger increase in μ is needed to reduce the same amount of free energy.

We next consider curvature generation in the constant area model. As the molecular mechanisms of curvature generation of the clathrin coat remains debated, we introduce a phenomenological model in which the free energy has the general form,

$$E_{\text{c}} = -\nu a_0^m c_0^n, \qquad [6]$$

where ν denotes the strength of curvature generation, m and n are two positive numbers that are associated with the molecular mechanisms of curvature generation. The free energy E_{c} in Eq. (6) decreases with increasing c_0, therefore, driving curvature generation. We set $m = 1$ such that E_{c} is proportional to

the coating area. Note that m cannot be zero, otherwise, E_c only depends on the intrinsic curvature c_0 and can be nonzero even when the coating area is zero. As for the power n of the intrinsic curvature c_0, we set $n = 1$ or 2 (called Model(1,1) and Model(1,2), respectively). Physically, Model(1,2) implies cooperativity in the curvature generation such that the reduction of free energy per increase of unit curvature is proportional to the current curvature, i.e., $\Delta E_c \propto -c_0 \Delta c_0$, while in Model(1,1), the reduction of free energy per increase of unit curvature is independent of current curvature. For Model(1,1), when ν is small, the total free energy $E_{tot} = E_b + E_t + E_c$ as a function of the intrinsic curvature c_0 has two minima, the lowest one at a small positive c_0 and the other one at the maximum c_0 where vesiculation occurs (Fig. 3c, red curve). Further curvature generation is strictly limited by the high energy barrier (sometimes more than $100 k_B T$) between the two minima. With increasing ν, the lowest minimum shifts to the vesiculation point, but the energy barrier still prevents curvature generation (Fig. 3c, orange line). For a large enough ν, the free energy monotonically decreases with c_0 and the curvature generation proceeds until vesiculation occurs (Fig. 3c, green curve). When the coating area a_0 is very small, vesiculation fails to occur even when the intrinsic curvature is increased to its maximum value (0.125nm^{-1}) (Fig. 3c, gray region). In the phase space of (a_0, ν), the critical value of ν where the energy barrier vanishes increases with the coating area a_0 (Fig. 3d, interface between the orange region and the green region), which implies that a larger clathrin coat needs a stronger strength of curvature generation to complete vesiculation.

Model(1,2) has similar free energy landscape as Model(1,1) (Compare Fig. 3c and e, d and f). However, in Model(1,2), for very small ν, the lowest free energy minimum is strictly pinned at $c_0 = 0$, which implies no spontaneous curvature generation. In contrast, the minimum is at a small positive c_0 in Model(1,1), which indicates slight curvature generation.

Determination of the vesiculation pathway from the energy landscape. In this section, we combine the assembly energy Eq. (5) and the curvature generation energy Eq. (6) together and calculate the total free energy $E_{tot}(a_0, c_0) = E_b + E_t + E_a + E_c$ as a function of both the coating area a_0 and the intrinsic curvature c_0. A pathway from the origin can be constructed by the descent along the negative gradient of the free energy landscape $-\nabla E_{tot}$. In Fig. 4a we show the free energy landscape for a fixed assembly strength ($\bar{\mu} = 0.6$) and varied reorganization strength ($\bar{\nu}$) for model(1,2). When ν is small, the energy contour lines near the origin are kinked, which represents an energy barrier that prevents the path from going up, i.e. from generating curvature. The path extends horizontally and terminates on the $a_0 - axis$ (Fig. 4a, first column, red curve). With increasing ν, the kinked contour lines shift towards larger a_0 and the path can be lifted up to $\bar{c}_0 > 0.1$ in the middle and drops to the $a_0 - axis$ in the end (Fig. 4a, second column, orange curve). Beyond a critical ν, the energy barrier vanishes and the path bends up and terminates on the vesiculation curve (Fig. 4a, third column, green curve). Further increasing μ leads to the path lifting up at a smaller coating area a_0 (Fig. 4a, fourth column, green curve). The path goes horizontally first and is later lifted up, which resembles the path of the constant area model. The three types of pathways are classified into three colored regions in the phase diagram of (μ, ν), which represent complete vesiculation (green), partial vesiculation (orange) and no vesiculation (red), respectively (Fig. 4c).

The free energy landscapes of Model(1,1) dramatically differs from Model(1,2). When ν is small, the energy gradient is strongly biased towards the horizontal direction, and the path extends horizontally with little or no curvature generation (Fig. 4b, first column). For an intermediate ν, the path first goes towards the top right direction until $\bar{c}_0 > 0.1$ and then slowly bends down and extends towards large coating area along a valley formed in the energy landscape, which corresponds to membrane shapes with a small dimple (Fig. 4b, second column). For large enough ν, the path shoots nearly straightly towards the top right direction before it reaches the vesiculation line (Fig. 4b, third column). Further increasing ν makes the path more straight and terminates at a smaller coating area (Fig. 4b, fourth column). The (μ, ν) phase diagram shows the parameter regions that lead to complete, partial or no vesiculation for Model(1,1) (Fig. 4d).

Comparison between different models with the experimental data. The constant area model and the constant curvature model represent two extreme pathways of membrane vesiculation. We have found constant-area-like pathways in Model(1,2) and straight-line-like pathways in Model(1,1). In order to understand which model is the most plausible, we compare membrane shapes predicted by the models with the membrane profiles obtained by electron microscopy in (7). The fitting error ϵ of a vesiculation path reflects the relative difference between the model-predicted geometric features along the path and the rolling median of the corresponding experimental data (Fig. 5a, see SI Appendix: rolling median calculation and error calculation). The fitting geometric features include neck width, tip radius and invagination depth (Fig. 5c). We draw the corresponding optimum energy paths that minimize the fitting error (Fig. 5b), and compare the best model-predicted shapes with the experimental ones (Fig. 5d).

For Model(1,2) and Model(1,1), the fitting parameters include the polymerization strength $\bar{\mu}$ and the reorganization strength $\bar{\nu}$ which together determine the vesiculation pathway, as well as the characteristic length L_0 which scales the size of the membrane. For Model(1,2), the best fits are obtained for $\bar{\mu} = 0.36$, $\bar{\nu} = 0.54$ and $L_0 = 30\text{nm}$ (Fig. 5a). The resulting path moves horizontally at first and then bents up vertically (Fig. 5b), which resembles the behavior of the constant area model. For Model(1,1), the best fitting parameters are $\bar{\mu} = 0.12$, $\bar{\nu} = 1.00$ and $L_0 = 40\text{nm}$ (Fig. 5a). The fitting path is almost a straight line towards the vesiculation line (Fig. 5b). The optimum fitting error of Model(1,2) ($\epsilon = 0.14$) is slightly better than that of Model(1,1) ($\epsilon = 0.17$).

We also perform the fitting procedure to the constant area model and find the optimum parameters are $a_0 = 1.69 \times 10^4 \text{nm}^2$ and $L_0 = 30\text{nm}$. For the constant curvature model, the best fitting parameters are $c_0 = 0.043\text{nm}^{-1}$ and $L_0 = 50\text{nm}$. The minimum fitting error of the constant curvature model ($\epsilon = 0.28$) is exactly twice as large as that of the constant area model ($\epsilon = 0.14$) (Fig.5a and b). So considering the fitting error and the pathway in (a_0, c_0) phase diagram, we raise the conclusion that the experimental vesiculation process probably favors constant-area-like pathways.

When comparing the model-predicted geometric features with the rolling median of the experimental data, we find that the four models fit almost equally well the experimental

data for the neck width(Fig. 5c left). Model(1,2) and the constant area model predict very similar results such that the curves almost overlap with each other (Fig. 5c, red curve and orange curve). The predictions of these two models match the rolling median of the experimental data best. The constant curvature model strongly deviates from the rolling median of the experimental tip radius, particularly in the early stage of vesiculation when $\psi_{\max} < 90^\circ$.

To compare the axisymmetric membrane shapes predicted by the models with the non-axisymmetric membrane profiles obtained with electron microscopy, we symmetrize the experimental data with a procedure (See SI Appendix: Fig. S3, symmetrization algorithm). Then, we average the symmetrized profile within an interval of $\psi_{\max} \in [\psi_0 - 10^\circ, \psi_0 + 10^\circ]$ and overlay the averaged profile with model-predicted shapes for $_{\max} = \psi_0$ (Fig. 5d). At the early stage when the membrane exhibits a dimple shape ($0^\circ < \psi_{\max} < 60^\circ$), the membrane morphology predicted by the constant curvature model is distinguishable from the other three models, particularly when looking at the tip radius. At the late stage when the membrane exhibits an Ω-shape, i.e., $\psi_{\max} > 90^\circ$, the difference in shape between models is mainly manifested in the invagination depth. The constant curvature model and Model(1,1) mainly predict a deeper invagination depth than the symmetrized experimental profile, while the constant area model and Model(1,2) usually give much better fitting.

Discussion

Three types of clathrin coats. In this paper, we have constructed a physical model to describe how curvature generation and clathrin assembly are interrelated during the vesiculation process in CME. Previous experiments have reported three groups of clathrin coated pits, which are plaques, abortive pits and pits that lead to vesiculation, according to their structural and dynamic properties (30, 53–57). In Fig. 4, we show that depending on the clathrin assembly strength μ and its reorganization strength ν, the pathway might end up with three possible final shapes: (i) a flat membrane with no curvature generation, (ii) a nearly flat membrane with small curvature generation, (iii) a spherical cap that leads to vesiculation. They essentially correspond to the three types of clathrin-coated pits found in experiments. Based on the phase diagram of Model(1,2) (Fig. 4c), the difference between the three groups comes from the difference in the assembly and reorganization strengths of clathrin molecules. Furthermore, Model(1, 2) predicts that at the boundary between the type (iii) region and the type (ii) region, the reorganization strength ν increases with the assembly strength. This result has important implications to explain why large plaques are commonly observed in experiments. The large area of the plaques are due to the strong assembly strength μ. However, for these plaques to go to vesiculation, a strong reorganization energy ν is also needed. Therefore, the combination of a strong μ and weak ν leads to the formation of large plaques. Model(1,2) predicts that a plaque or an abortive pit can be transformed into a vesicle by either increasing the reorganization strength or reducing the assembly strength (Fig. 6). The former ends up with a large vesicle and the latter ends up with a small vesicle. This can be used as a test of our theory with experiments to modify the binding affinity of clathrin molecules with adaptor proteins on the membrane. Weakening the affinity might increase the portion of vesicles and reduce the portion of plaques, though the vesicles would become smaller.

Cooperativity in the curvature generation process. In Fig. 5, we show the best fitting results for all the four models and find that Model(1,2) produces better fits than Model(1,1), which suggests the existence of cooperativity in the curvature generation process. In particular, if curvature generation is driven by breaking bonds in the hexagonal lattice, cooperativity implies that the number of newly broken bonds is proportional to the number of already broken bonds. Because of this cooperativity, at the early stage of endocytosis bonds are broken slowly and clathrin assembly dominates over curvature generation. At the late stage of endocytosis, an increasing number of bonds are broken and curvature generation could happen rapidly and dominate over clathrin assembly. Altogether, this cooperativity leads to a constant-area-like behavior. Similar effect have been reported in (36).

The difference in membrane morphology between the different models is most salient at the early stage of endocytosis. When we compare the model predictions, we find that the difference in membrane morphology between models is not as big as expected, which might explain why it has been difficult to distinguish between the constant area and the constant curvature models for so long. For instance, the neck width vs. $\psi_{\max}$ and the invagination depth vs. $\psi_{\max}$ are similar for all the four models (Fig. 5c, left and right). The best fitting error of the four models calculated from the geometric features are relatively close, except for the constant curvature model, which gives the worst fit (Fig. 5 a). The models are mainly distinguishable from the tip radius vs. $\psi_{\max}$ plot at the early stage of endocytosis when the membrane is nearly flat (Fig. 5c, middle), i.e. for shapes with small $\psi_{\max}$. However, published experimental shape at early stages of endocytosis are sparse. Our result hints that in order to distinguish between the models, collecting membrane shapes at the early stage is necessary and the relation of tip radius vs. $\psi_{\max}$ is the key geometric feature to tell the models apart.

The projected area of clathrin coat in the plane of the plasma membrane could distinguish between the two models. In Fig. 2d and e we have shown that the coat radius R_{coat}, which represents the projected area of the clathrin coat in the plane of the plasma membrane, as a function of $\psi_{\max}$ exhibit opposite trends for the constant curvature model and the constant area model. The results suggest that in experiments the projected area for the constant area model would first increase and then decrease over time, finally reaching a plateau. However, for the constant curvature model, the projected area would increase over time and finally reach a plateau without a decreasing phase. This result suggests another method to distinguish between the two models via the projected area measurement. The idea has been used in a study where the clathrin-coated pit was imaged with platinum replica and cryo-electron microscopy and tomography (18). The results support a constant-area-like model, consistent with the prediction of our Model(1,2), in which the dome structures have a slightly larger coating area than flat structures. On the other hand, another study has used the super-resolved live cell fluorescence imaging with TIRF to measure the growth of the clathrin coat over time (39). The authors found a smooth drop in the

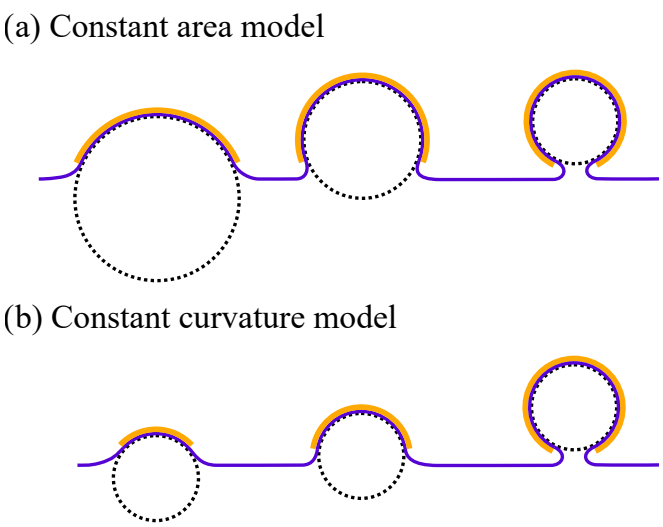

Fig. 1. Schematic illustrations of the constant area model (a) and the constant curvature model (b) for CME. Blue: plasma membrane, yellow: clathrin coat, black dashed line: curvature of the clathrin coat

projected area of clathrin coat over time. However, based on a computer simulation of clathrin assembly, they concluded that the smooth drop of the projected area was the result of a constant-curvature-like model because a constant-area-like model would produce a sharp drop. We attribute the difference between their model and our model to the fact that they model the clathrin coat as a discrete lattice while we use a continuum mechanics method. More importantly, in their model, the moment at which curvature generation occurs was arbitrarily imposed at 80% of clathrin triskelions. If the transition were chosen to occur with fewer triskelions, e.g. 40%, the sharp drop in the project area might not happen in the constant-area-like model. Furthermore, the authors used the number of triskelions to monitor the progress of endocytosis which terminates when the triskelions reach the maximum number. This choice might bias towards the constant-curvature-like model because the vesiculation may not happen at all when the clathrin numbers reaches its maximum.

The bending rigidity of the coated area should be much larger than the uncoated area. Comparison of our model to experimental data demonstrates that the relative bending rigidities of the coat and the membrane are constrained. Indeed, if $\kappa_{\rm coat}/\kappa_{\rm bare} < 50$, the model predicts an abrupt change (or a gap) in $\psi_{\rm max}$ at the end of vesiculation (See SI Appendix, Fig. S1, gap of the maximum angle), i.e., a snap-through transition reported in (44). If a gap in $\psi_{\rm max}$ existed, we would expect that the distribution of experimental shapes to be discontinuous, with no or very few data corresponding to a certain range of ψ. However, in the experiments from (7), the endocytic pits shapes are continuously distributed across the $_{\rm max}$ spectrum, indicating the ergodicity of $\psi_{\rm max}$ during the endocytic process. Our calculation suggests that the clathrin coat is about 50 times stiffer than the membrane.

ACKNOWLEDGMENTS. We thank Prof. Ori Avinoam and Marko Kaksonen for generously sharing their data with us. R.M. acknowledges financial support from Fundamental Research Funds for Central Universities of China under Grant No. 20720240144. Part of this work was funded by NIH R01 grant GM115636 awarded to J.B.

Table 1. List of default parameters in the model.

Symbols	Meaning	Value	Unit
$\kappa_{\rm bare}$	Bending rigidity of uncoated area	20	$k_{\rm B}T$
$\kappa_{\rm coat}$	Bending rigidity of coated area	1000	$k_{\rm B}T$
$\sigma_{\rm e}$	Membrane tension at the base	0.025	$\rm pN\cdot nm^{-1}$
$R_{\rm b}$	Boundary radius	5	L_0
α	Sharpness of the step function	10	$(2\pi L_0^2)^{-1}$

1. HT McMahon, E Boucrot, Molecular mechanism and physiological functions of clathrin-mediated endocytosis. *Nat. Rev. Mol. Cell Biol.* **12**, 517–533 (2011).
2. A Sorkin, MA Puthenveedu, *Clathrin-Mediated Endocytosis*, eds. Y Yarden, G Tarcic. (Springer New York, New York, NY), pp. 1–31 (2013).
3. R Lu, DG Drubin, Y Sun, Clathrin-mediated endocytosis in budding yeast at a glance. *J. Cell Sci.* **129**, 1531–1536 (2016).
4. M Kaksonen, A Roux, Mechanisms of clathrin-mediated endocytosis. *Nat. Rev. Mol. Cell Biol.* **19**, 313–326 (2018).
5. MM Lacy, R Ma, NG Ravindra, J Berro, Molecular mechanisms of force production in clathrin-mediated endocytosis. *FEBS Lett.* **0** (2018).
6. M Mettlen, PH Chen, S Srinivasan, G Danuser, SL Schmid, Regulation of clathrin-mediated endocytosis. *Annu. Rev. Biochem.* **87**, 871–896 (2018) PMID: 29661000.
7. O Avinoam, M Schorb, CJ Beese, JAG Briggs, M Kaksonen, Endocytic sites mature by continuous bending and remodeling of the clathrin coat. *Science* **348**, 1369–1372 (2015).
8. A Musacchio, et al., Functional organization of clathrin in coats. *Mol. Cell* **3**, 761–770 (1999).
9. BI Shraiman, On the role of assembly kinetics in determining the structure of clathrin cages. *Biophys. J.* **72**, 953–957 (1997).
10. A Fotin, et al., Molecular model for a complete clathrin lattice from electron cryomicroscopy. *Nature* **432**, 573–579 (2004).
11. YF Cheng, W Boll, T Kirchhausen, SC Harrison, T Walz, Cryo-electron tomography of clathrin-coated vesicles: Structural implications for coat assembly. *J. Mol. Biol.* **365**, 892–899 (2007).
12. PN Dannhauser, EJ Ungewickell, Reconstitution of clathrin-coated bud and vesicle formation with minimal components. *Nat. Cell Biol.* **14**, 634–+ (2012).
13. J Heuser, Three-dimensional visualization of coated vesicle formation in fibroblasts. *J. Cell Biol.* **84**, 560–583 (1980).
14. ZM Chen, SL Schmid, Evolving models for assembling and shaping clathrin-coated pits. *J. Cell Biol.* **219** (2020).
15. F Frey, US Schwarz, Competing pathways for the invagination of clathrin-coated membranes. *Soft Matter* **16**, 10723–10733 (2020).
16. BL Scott, et al., Membrane bending occurs at all stages of clathrin-coat assembly and defines endocytic dynamics. *Nat. Commun.* **9** (2018).
17. JE Heuser, RG Anderson, Hypertonic media inhibit receptor-mediated endocytosis by blocking clathrin-coated pit formation. *J. Cell Biol.* **108**, 389–400 (1989).
18. KA Sochacki, et al., The structure and spontaneous curvature of clathrin lattices at the plasma membrane. *Dev. Cell* **56**, 1131–+ (2021).
19. F Aguet, et al., Membrane dynamics of dividing cells imaged by lattice light-sheet microscopy. *Mol. biology cell* **27**, 3418–3435 (2016).
20. JP Ferguson, et al., Deciphering dynamics of clathrin-mediated endocytosis in a living organism. *J. Cell Biol.* **214**, 347–358 (2016).
21. V Sirotkin, et al., Quantitative analysis of the mechanism of endocytic actin patch assembly and disassembly in fission yeast. *Mol. Biol. Cell* **21**, 2894–2904 (2010) PMID: 20587778.
22. MJ Taylor, D Perrais, CJ Merrifield, A high precision survey of the molecular dynamics of mammalian clathrin-mediated endocytosis. *Plos Biol.* **9** (2011).
23. W Kukulski, A Picco, T Specht, JA Briggs, M Kaksonen, Clathrin modulates vesicle scission, but not invagination shape, in yeast endocytosis. *Elife* **5**, e16036 (2016).
24. M Kaksonen, CP Toret, DG Drubin, Harnessing actin dynamics for clathrin-mediated endocytosis. *Nat. Rev. Mol. Cell Biol.* **7**, 404–414 (2006).
25. F Balzarotti, et al., Nanometer resolution imaging and tracking of fluorescent molecules with minimal photon fluxes. *Science* **355**, 606–612 (2017).
26. KC Gwosch, et al., Minflux nanoscopy delivers 3d multicolor nanometer resolution in cells. *Nat. methods* **17**, 217–224 (2020).
27. R Schmidt, et al., Minflux nanometer-scale 3d imaging and microsecond-range tracking on a common fluorescence microscope. *Nat. communications* **12**, 1478 (2021).
28. W Kukulski, M Schorb, M Kaksonen, JAG Briggs, Plasma membrane reshaping during endocytosis is revealed by time-resolved electron tomography. *Cell* **150**, 508–520 (2012).
29. E Cocucci, F Aguet, S Boulant, T Kirchhausen, The first five seconds in the life of a clathrin-coated pit. *Cell* **150**, 495–507 (2012).
30. D Loerke, et al., Cargo and dynamin regulate clathrin-coated pit maturation. *PLOS Biol.* **7**, 1–12 (2009).
31. A Picco, M Mund, J Ries, F Nédélec, M Kaksonen, Visualizing the functional architecture of the endocytic machinery. *eLife* **4**, e04535 (2015).
32. C Kural, T Kirchhausen, Live-cell imaging of clathrin coats in *Methods in enzymology*. (Elsevier) Vol. 505, pp. 59–80 (2012).
33. M Mund, et al., Systematic nanoscale analysis of endocytosis links efficient vesicle formation to patterned actin nucleation. *Cell* **174**, 884–+ (2018).
34. R Arasada, WA Sayyad, J Berro, TD Pollard, High-speed superresolution imaging of the proteins in fission yeast clathrin-mediated endocytic actin patches. *Mol. Biol. Cell* **29**, 295–303 (2018).

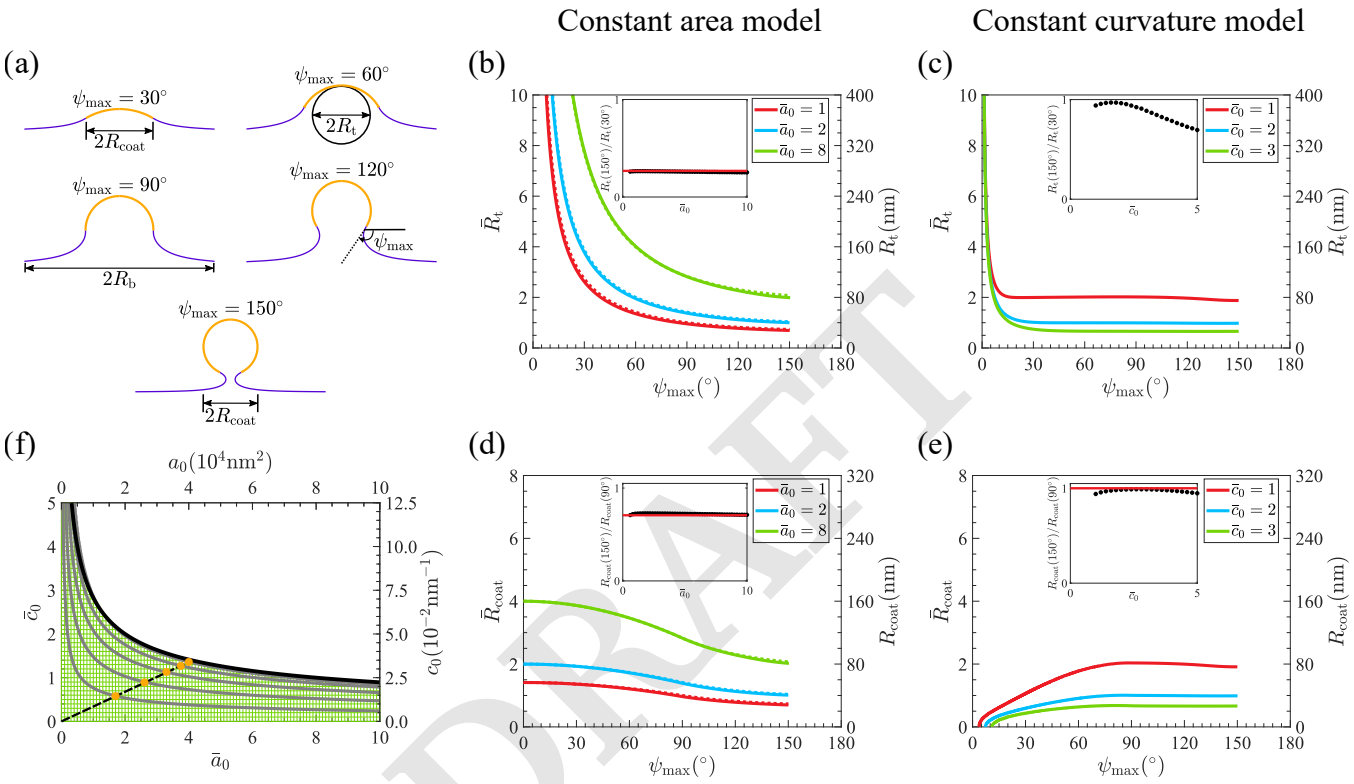

Fig. 2. Evolution of membrane morphology and phase diagram of vesiculation in the (a_0, c_0) parameter space. (a) Membrane shapes at different stages of invagination and definition of some variables used in this paper. We define the distance from the axisymmetric axis to the edge of the coating area as $R_{\rm coat}$, the radius of the tangential curvature circle at the tip of the shape as $R_{\rm t}$, and the distance from axisymmetric axis to the boundary as $R_{\rm b}$. The maximum tangential angle of the cross section contour is $_{\max}$. (b,c) Tip radius $R_{\rm t}$ vs. maximal angle $\psi_{\max}$ for the constant area model in (b) and for the constant curvature model in (c). Dotted lines in (b) denote the analytical solutions. Insets show the ratio of the tip radii $R_{\rm t}$ at $\psi_{\max} = 150^\circ$ and $\psi_{\max} = 30^\circ$. The inset dark dots denotes the numerical results and the red line is the analytical solution (See SI Appendix: model fitting). (d,e) Coat radius $R_{\rm coat}$ vs. maximal angle $\psi_{\max}$ for the constant area model in (d) and for the constant curvature model in (e). Dotted lines in (d) denote the analytical solutions. Insets show the ratio of the coat radius $R_{\rm coat}$ at $\psi_{\max} = 150^\circ$ and $\psi_{\max} = 90^\circ$. The inset dark dots denotes the numerical results and the red lines are the analytical ones (See SI Appendix: model fitting). (f) Vesiculation diagram in the phase space of (a_0, c_0). Each horizontal line represents a path of the constant curvature model and each vertical line represents a path of the constant area model. Each path terminates when $\psi_{\max} = 150^\circ$. The solid grey lines represent contours of $\psi_{\max} = 30^\circ, 60^\circ, 90^\circ, 120^\circ, 150^\circ$, respectively. The solid black line is the analytical results for the vesiculation line $\bar{a}_0\bar{c}_0^2 = 8$ (See SI Appendix: critical vesiculation curve). The dashed black line is a random-picked straight line connecting the origin and the vesiculation boundary. The intersections of the dashed black line and the gray lines are plotted in orange dots and they are the coordinates of (a_0, c_0) where the five shapes in (a) are located. Shapes are arranged in an increasing order of $\psi_{\max}$ in (a). (b-e) Parameters with a bar over them (left vertical axes) are normalized to be dimensionless, and the dimensional parameters (right vertical axes) are calculated by one of the typical fitting values $L_0 = 40{\rm nm}$ (Fig. 5)

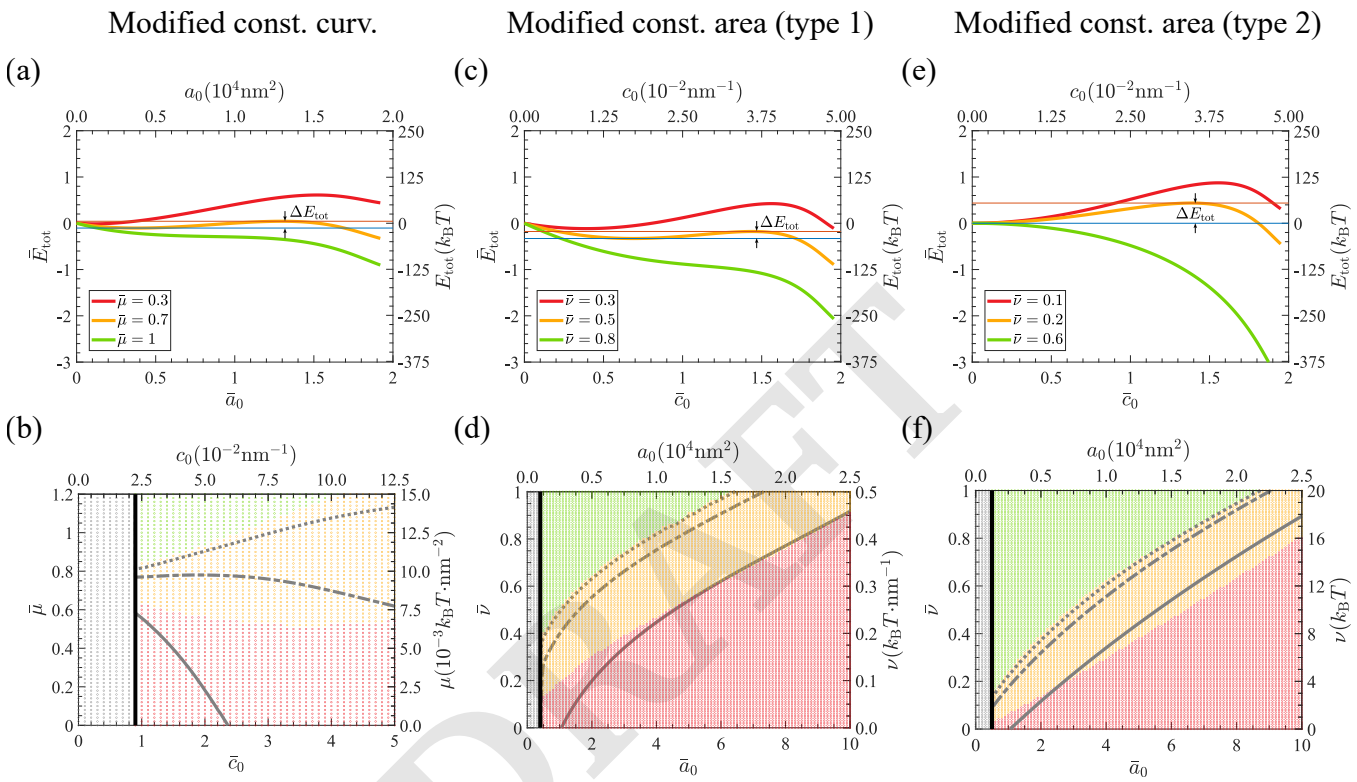

Fig. 3. Free energy evolution in the constant curvature and constant area models when accounting for one of either the polymerization energy term $E_{\mathrm{a}}=-\mu a_0$ or the curvature generation energy term $E_{\mathrm{c}}=-\nu a_0 c_0$ (type 1) and $E_{\mathrm{c}}=-\nu a_0 c_0^2$ (type 2). (a,b) Free energy landscape of the modified constant curvature model where $\bar{c}_0=2$ with polymerization energy $E_{\mathrm{a}}=-\mu a_0$ in (a) and the corresponding phase diagram in the phase space of (c_0,μ) in (b). The rightmost endpoint of each curve is the vesiculation point where $\psi_{\max}=150^\circ$. The red line in (a) and red dots in (b) correspond to pathways with minimum free energy E_{tot} appearing at a point other than the vesiculation point on the $E_{\mathrm{tot}}-\bar{a}_0$ curve. The orange line in (a) and the orange dots in (b) correpsond to pathways where the vesiculation point is the minimum free energy point, but an energy barrier still exists. The green line in (a) and green dots in (b) correspond to vesiculation pathways without an energy barrier. The energy barrier ΔE_{tot} is defined as the energy difference between the maximum point and the first minimum point before the maximum. ΔE_{tot} of the orange curve is shown in (a) as a typical example. The gray dots in the left-hand side of (b) correspond to pathways that numerically fail to reach the vesiculation point when $\bar{a}_0$ reaches its upper limit 10. (c,d) Free energy landscape of the modified constant area model where $\bar{a}_0=2$ with curvature generation energy $E_{\mathrm{c}}=-\nu a_0 c_0$ in (c) as a function of the intrinsic curvature c_0 and the corresponding phase diagram in the phase space of (a_0,ν) in (d). The gray dots in the left-hand side of (d) correspond to pathways that numerically fail to reach the vesiculation point when $\bar{c}_0$ reaches its upper limit 5. (e,f) Free energy landscape of the modified constant area model where $\bar{a}_0=2$ with $E_{\mathrm{c}}=-\nu a_0 c_0^2$ in (e) and the corresponding phase diagram in the phase space of (a_0,ν) in (f). The gray dots in the left-hand side of (f) correspond to pathways that numerically fail to reach the vesiculation point when $\bar{c}_0$ reaches its upper limit 5. (a-f) The parameters with a bar over them are normalized to be dimensionless, and the dimensional parameters are calculated using one of the typical fitting values $L_0=40\mathrm{nm}$ (Fig. 5). (b,d,f) The black line separates the region wiht gray dots (which did not numerically reach vesicultion) from the other regions. The dotted, dash-dotted and solid gray lines respectively represent the paths where $\Delta E_{\mathrm{tot}}=1k_{\mathrm{B}}T$, $\Delta E_{\mathrm{tot}}=10k_{\mathrm{B}}T$, $\Delta E_{\mathrm{tot}}=100k_{\mathrm{B}}T$.

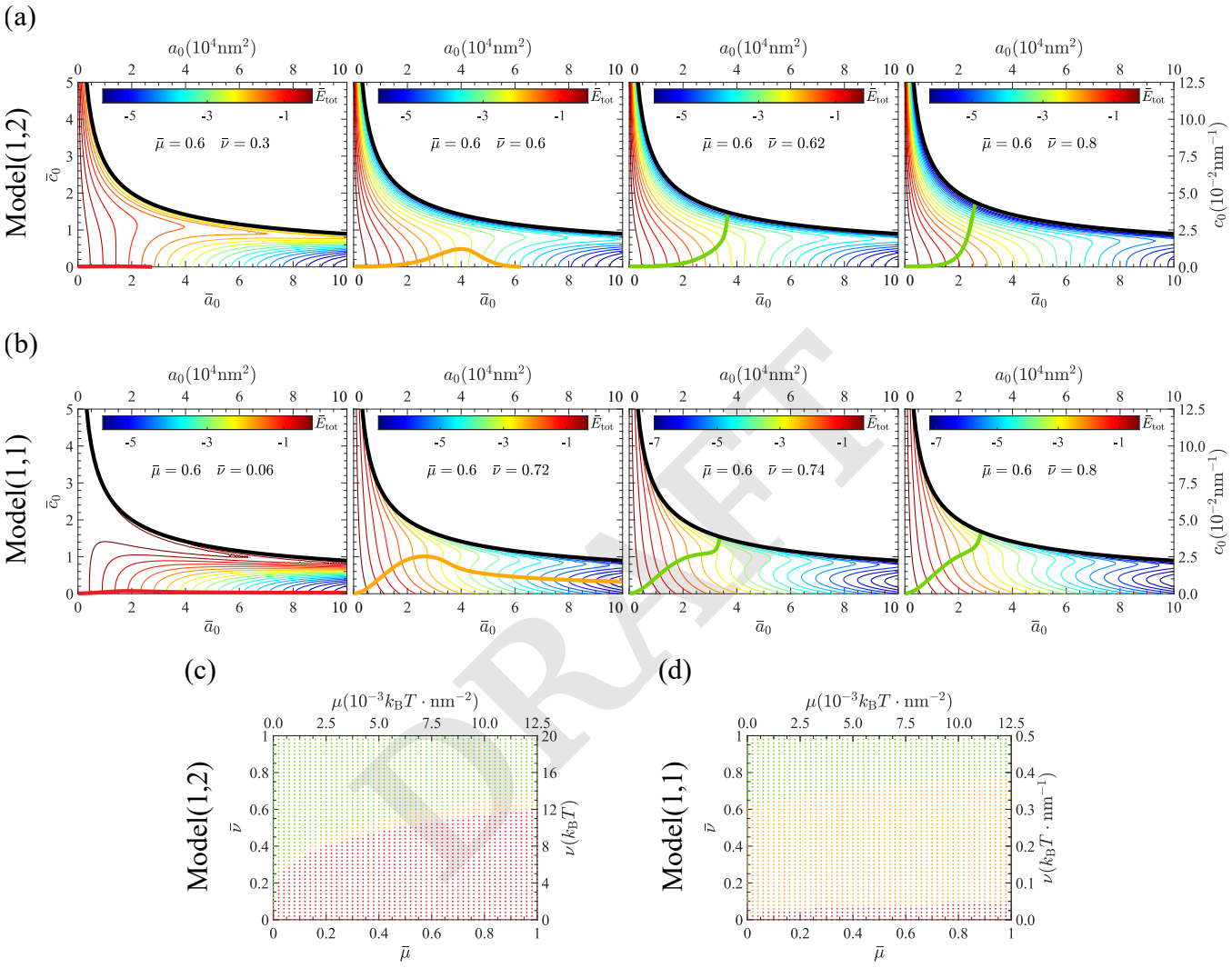

Fig. 4. Vesiculation phase diagram when accounting for both the polymerization energy μ and the reorganization energy ν. (a,b) Free energy landscape for Model(1,2) (i.e. with reorganization energy $E_c=-\nu a_0^1 c_0^2$) in (a) and Model(1,1) (i.e. with reorganization energy $E_c=-\nu a_0^1 c_0^1$) in (b). Thick black lines are the analytical solutions for the vesiculation boundary. Thin rainbow-colored lines visually represent the energy landscape (values of the color bar are for the dimensionless free energy scale). Thick colored-lines represent pathways that stream along the negative gradient of the free energy landscape in the phase space starting from the origin (i.e. no clathrin assembled and no curvatuve). Our model shows that only a subset of suitable (μ,ν) values create pathways that lead to vesiculation, i.e. that reach the thick black line (thick green lines in the third and fourth panels). The orange and red curves are pathways that fail to reach vesiculation. The red curve does not produce any curvature, while the orange curve generates a small curvature but never leads to vesiculation. (c,d) Phase diagrams for Model(1,2) in (c) and Model(1,1) in (d) show the relationship between pathway types and the (μ,ν) values. The colors of the dots correspond to the same types of pathways as represented by thick colored lines in (a,b). Our results show that larger μ or ν values lead to an easier vesiculation. Parameters with a bar over them are normalized to be dimensionless, and the dimensional parameters are calculated using one of the typical fitting values $L_0=40\mathrm{nm}$ (Fig. 5).

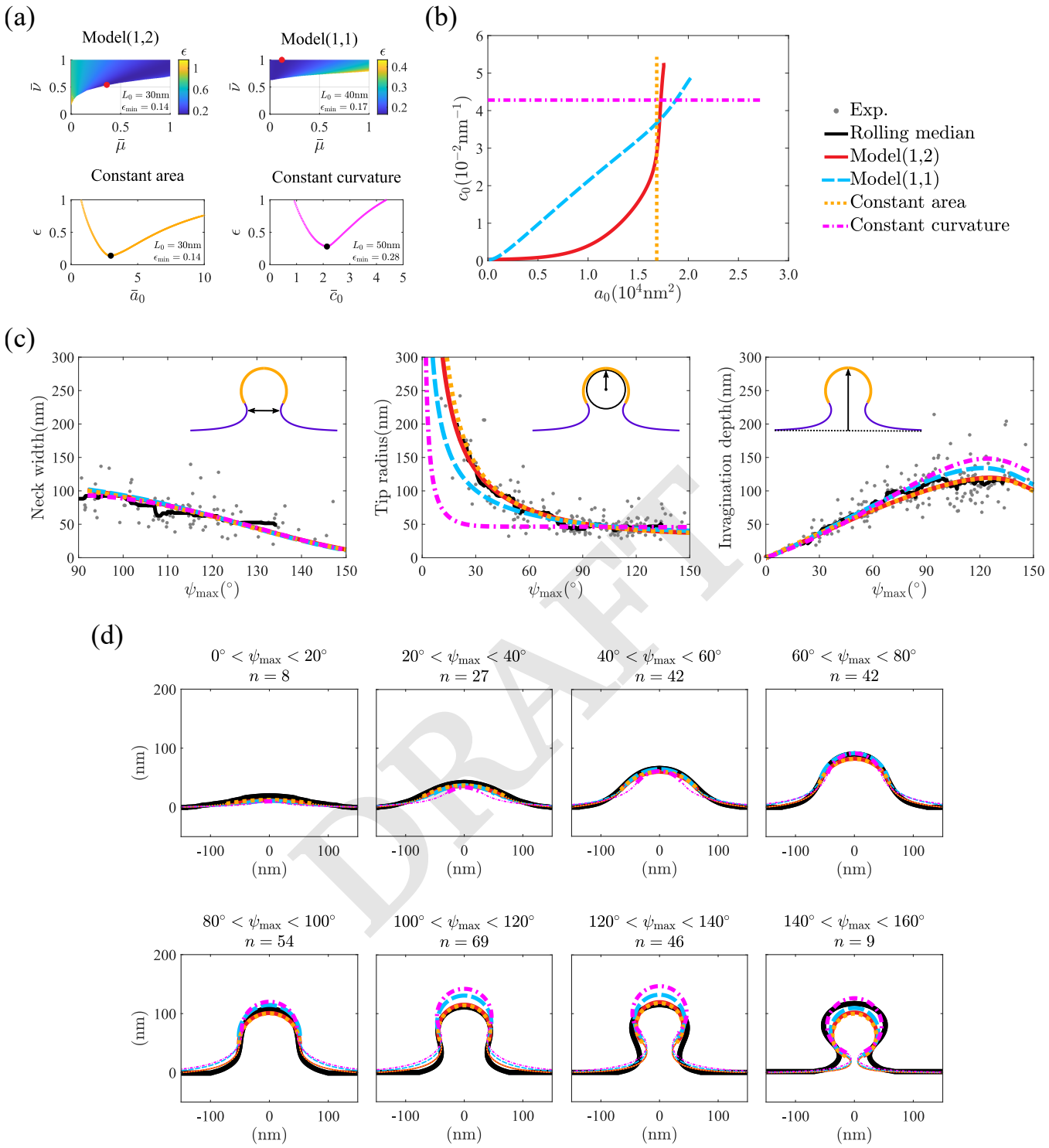

Fig. 5. Comparison between our theory and experimental data from mammalian cells. (a) Parameter fit of the best of the four models (constant curvature model, constant area model, Model(1,1), Model(1,2)) to obtain the minimum error ϵ. Fitting procedure of Model(1,1) and Model(1,2) consider the total free energy $E_{\rm tot} = E_{\rm b} + E_{\rm t} + E_{\rm a} + E_{\rm c}$, while the fitting of the constant area model and the constant curvature model consider $E_{\rm tot} = E_{\rm b} + E_{\rm t}$. The optimized parameters are $\bar{a}_0 \in [0, 10]$ for the constant area model, $\bar{c}_0 \in [0, 5]$ for the constant curvature model, $\bar{\mu} \in [0, 1]$ and $\bar{\nu} \in [0, 1]$ for model(m,n), and $L_0 \in [10{\rm nm}, 100{\rm nm}]$ within an interval of $10{\rm nm}$ in the four models. We only assign fitting errora to the parameter sets that lead to vesiculation and only plot the error figure for the best L_0. (b) Vesiculation pathways with minimum fitting error in the four models. In each model, we use the best L_0 value from (a) to obtain the dimensional scale of the (a_0, c_0) phase space. (c) Comparison of model fits and experimental data for three geometric features: neck width, tip radius ($R_{\rm t}$) and invagination depth. Neck width is calculated as the distance between the left and right parts of the shape for $\psi_{\rm max} = 90^\circ$, and the invagination depth is measured as the height from the base to the tip of the invagination. (d) Comparison between the model-predicted shapes and the experimental shapes. Experimental membrane shapes for mammalian cells are grouped according to their maximum angle as a proxy for the different stages of CME. The number of experimental shapes falling in a certain $\psi_{\rm max}$ range is defined as n. The black lines are the average experimental shapes after symmetrization. The model-predicted shapes are calculated by the midpoint value of each $\psi_{\rm max}$ interval. (c,d) The curves predicted by theory are shown with colored lines, and experimental data is shown with gray dots and black lines. Parameters with a bar over them are non-dimensionalized. The detailed procedure to treat the experimental data can be found in the supplement: symmetrization algorithm, rolling median calculation and error calculation.

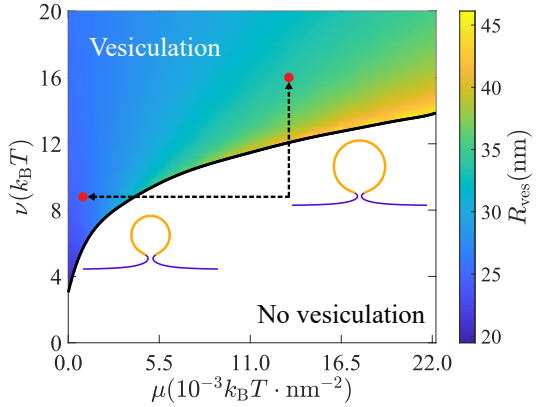

Fig. 6. Tip radius of vesiculaion shapes ($R_{\rm ves}$) in Model(1,2). The colored region shows the (μ,ν) sets that lead to vesiculation, and brighter colors correspond to larger $R_{\rm ves}$. Decreasing assembly strength μ or increasing reorganization strength ν might lead to vesiculation of different vesicle sizes. An example from $(\mu,\nu)=(13.3\times10^{-3}k_{\rm B}T\cdot{\rm nm}^{-2},8.8k_{\rm B}T)$ to the vesiculation region is marked by arrows, red dots and corresponding vesicle shapes. The characteristic length $L_0=30{\rm nm}$ is used in the calculation.

35. KA Sochacki, AM Dickey, MP Strubl, JW Taraska, Endocytic proteins are partitioned at the edge of the clathrin lattice in mammalian cells. *Nat. Cell Biol.* **19**, 352–+ (2017).
36. M Mund, et al., Clathrin coats partially preassemble and subsequently bend during endocytosis. *J. Cell Biol.* **222**, e202206038 (2023).
37. D Bucher, et al., Clathrin-adaptor ratio and membrane tension regulate the flat-to-curved transition of the clathrin coat during endocytosis. *Nat. Commun.* **9** (2018).
38. KA Sochacki, JW Taraska, From flat to curved clathrin: Controlling a plastic ratchet. *Trends Cell Biol.* **29**, 241–256 (2019).
39. NM Willy, et al., De novo endocytic clathrin coats develop curvature at early stages of their formation. *Dev. Cell* **56**, 3146–+ (2021).
40. F Frey, et al., Eden growth models for flat clathrin lattices with vacancies. *New J. Phys.* **22** (2020).
41. T Kirchhausen, D Owen, SC Harrison, Molecular structure, function, and dynamics of clathrin-mediated membrane traffic. *Cold Spring Harb. Perspectives Biol.* **6** (2014).
42. Y Fu, ME Johnson, Modeling membrane reshaping driven by dynamic protein assemblies. *fu2023 opinion structural biology* **78**, 102505 (2023).
43. MJ Varga, Y Fu, S Loggia, ON Yogurtcu, ME Johnson, Nerdss: a nonequilibrium simulator for multibody self-assembly at the cellular scale. *Biophys. J.* **118**, 3026–3040 (2020).
44. JE Hassinger, G Oster, DG Drubin, P Rangamani, Design principles for robust vesiculation in clathrin-mediated endocytosis. *Proc. Natl. Acad. Sci.* **114**, E1118–E1127 (2017).
45. R Ma, J Berro, Endocytosis against high turgor pressure is made easier by partial protein coating and a freely rotating base. *Biophys. J.* **120**, 52a (2021).
46. N Walani, J Torres, A Agrawal, Endocytic proteins drive vesicle growth via instability in high membrane tension environment. *Proc. Natl. Acad. Sci.* **112**, E1423–E1432 (2015).
47. A Agrawal, DJ Steigmann, Modeling protein-mediated morphology in biomembranes. *Biomech. Model. Mechanobiol.* **8**, 371 (2008).
48. P Rangamani, A Agrawal, KK Mandadapu, G Oster, DJ Steigmann, Interaction between surface shape and intra-surface viscous flow on lipid membranes. *Biomech. modeling mechanobiology* **12**, 833–845 (2013).
49. Y Fu, et al., An implicit lipid model for efficient reaction-diffusion simulations of protein binding to surfaces of arbitrary topology. *The J. Chem. Phys.* **151**, 124115 (2019).
50. Y Fu, WF Zeno, JC Stachowiak, ME Johnson, Mechanical feedback in protein recruitment to membranes. *Biophys. J.* **120**, 145a (2021).
51. W Helfrich, Elastic properties of lipid bilayers: theory and possible experiments. *Zeitschrift für Naturforschung C* **28**, 693–703 (1973).
52. I Derényi, F Jülicher, J Prost, Formation and interaction of membrane tubes. *Phys. Rev. Lett.* **88**, 238101 (2002).
53. P Maupin, TD Pollard, Improved preservation and staining of HeLa cell actin filaments, clathrin-coated membranes, and other cytoplasmic structures by tannic acid-glutaraldehyde-saponin fixation. *J. Cell Biol.* **96**, 51–62 (1983).
54. M Ehrlich, et al., Endocytosis by random initiation and stabilization of clathrin-coated pits. *Cell* **118**, 591–605 (2004).
55. S Saffarian, T Kirchhausen, Distinct dynamics of endocytic clathrin coated pits and coated plaques. *Biophys. J.* **96**, 569a–570a (2009).
56. T Kirchhausen, Imaging endocytic clathrin structures in living cells. *Trends Cell Biol.* **19**, 596–605 (2009).
57. M Lampe, S Vassilopoulos, C Merrifield, Clathrin coated pits, plaques and adhesion. *J. Struct. Biol.* **196**, 48–56 (2016).